

# VLT diffraction-limited imaging at 11 and 18 $\mu\text{m}$ of the nearest active galactic nuclei <sup>\*</sup>

J. Reunanen<sup>1</sup>, M. A. Prieto<sup>2</sup>, R. Siebenmorgen<sup>3</sup>

<sup>1</sup>*Tuorla Observatory, University of Turku, FI-21500 Piikkiö, Finland; reunanen@ftml.net*

<sup>2</sup>*Instituto de Astrofísica de Canarias, C/ Vía Láctea, 38205 La Laguna, Spain; aprieto@iac.es*

<sup>3</sup>*European Southern Observatory, Karl-Schwarzschild-Strasse 2, D-85748 Garching bei München, Germany*

## ABSTRACT

Mid-infrared (IR) imaging at resolutions of 300 mas of the central kpc region of 13 nearby, well-known active galaxies is presented. The bulk of the mid-IR emission is concentrated on an unresolved central source within a size of less than 5 to 130 pc, depending on the object distance. Further resolved emission is detected in 70% of the sample in the form of circumnuclear star-forming rings or diffuse nuclear extended emission. In the three cases with circumnuclear star formation, the stellar contribution is at least as important as that of the AGN. In those with extended nuclear emission – a third of the sample – this emission represents a few per cent of the total measured; however, this contribution may be underestimated because of the chopped nature of these observations. This extended emission is generally collimated in a preferential direction often coinciding with that of the extended ionized gas or the jet. In M87 and Cen A, where the emission extends along their respective jets, the emission is presumably synchrotron. In Circinus, NGC 1386 and NGC 3783, it can be reconciled with thermal emission from dust heated at about 100 K by the active nucleus.

In all cases, the nuclear fluxes measured at 11.8  $\mu\text{m}$  and 18.7  $\mu\text{m}$  represent a minor contribution of the flux levels measured by large aperture *IRAS* data at the nearest energy bands of 12 and 25  $\mu\text{m}$ . This contribution ranges from 30% to less than 10%. In only three cases do the active galactic nucleus (AGN) fluxes agree with *IRAS* to within a factor of 2. In the AGNs with strong circumnuclear star formation, this component can well account for most of the *IRAS* flux measured in these objects. But in all other cases, either a low surface brightness component extending over galactic scales or strong extra-nuclear IR sources – e.g. H II regions in spiral arms – have to be the main source of the *IRAS* emission. In either case, the contribution of these components dwarfs that of the AGN at mid-IR wavelengths.

**Key words:** galaxies:active, galaxies:Seyfert, galaxies:nuclei, infrared:galaxies

## 1 INTRODUCTION

With the advent of interferometry and adaptive optics techniques in the infrared (IR) in large ground-based telescopes, the central regions of active galactic nuclei (AGN) are being studied in ever-increasing detail. The best details have so far been seen on the brightest and nearest AGN observed with the Very Large Telescope (VLT). Here is a list. The nucleus of NGC 1068 is resolved into a parsec-scale disc in near-IR (Weigelt et al. 2004) and mid-IR (Jaffe et al. 2004) interferometry observations. That of Circinus is also resolved into a parsec-scale disc-like structure perpendicular to the ionization cone in adaptive optics images in the near IR (Prieto

et al. 2004), the results being further confirmed by interferometry in the mid-IR (Tristram et al. 2008). In both cases, the resolved nuclear structure fits within the characteristics of a parsec-scale torus. The nucleus of Cen A, however, is so far unresolved down to scales of less than a parsec in adaptive optics images in the near IR (Haring-Neumayer et al. 2006) and interferometry in the mid-IR (Meisenheimer et al. 2007). Other bright AGN observed with adaptive optics in the near IR show an unresolved nucleus, so far, down to scales of tens of parsecs (Prieto et al. 2007), and from those that could be targeted with interferometry in the mid-IR, the available data indicate a resolved nuclear structure,  $\sim 2$  pc in size, and NGC 4151, and possible resolved emission in NGC 1365, NGC 3783 and NGC 7469 (Tristram et al. 2009). The torus structure may be larger than a few parsecs at mid-IR wavelengths, where dust heated by the AGN to

<sup>\*</sup> Based on observations collected at the European Southern Observatory, VLT programs 076.B-0599, 077.B-0728

blackbody equivalent temperatures of 100–300 K may exist at larger radii. One of the problems is that this outermost region may be fully resolved with interferometry and thus will escape detection.

This work presents diffraction-limited VLT observations at 11.8  $\mu\text{m}$  and 18.7  $\mu\text{m}$  of a sample of the nearest and brightest AGN accessible from Paranal Observatory. The resolutions achieved are a factor 10 lower than those provided by VLT-MIDI interferometry, but are more sensitive to possible extended structures around the nucleus (e.g. Perlman et al. 2001; Siebenmorgen et al. 2008); at the very least, they allow for setting an upper limit to the outer radius of the torus. At the higher resolution achieved in these observations (FWHM = 0.3 arcsecs) this upper-limit radius in the sample galaxies is 35 pc on average (ranging from 5 to 130 pc).

This paper is part of a major project focusing on the study of the central few parsecs of the nearest AGN at optical, IR and radio wavelengths, using the highest spatial resolution data available today. The sample galaxies have been extensively studied across all ranges of the electromagnetic spectrum. For all these objects VLT subarcsec resolution observations, by means of adaptive optics in the 1 to 5  $\mu\text{m}$  range (Prieto et al. 2009), and at 11.9 and 18.7  $\mu\text{m}$  (this work) were collected. These data are complemented with *HST* optical information available for all sources, and VLA and/or ATCA data at subarcsec resolution (Oriente & Prieto 2009). At the distance of the sample galaxies, the spatial scales at which the nuclear regions are studied range from a few pc in the optical, near-IR and radio to several tens of parsecs in the mid-IR. A comprehensive study of the spectral energy distribution of these AGN using all the available high spatial resolution data is presented in Prieto et al. (2009).

Throughout this paper,  $H_0 = 71 \text{ km s}^{-1} \text{ Mpc}^{-1}$  is used.

## 2 OBSERVATIONS AND DATA REDUCTION

The basic properties of the AGN sample are shown in Table 1. The galaxies were observed with the  $256 \times 256$  pixel VLT Imager and Spectrometer for mid Infrared (VISIR; Lagage et al. 2004 with the pixel scale of 0.075 arcsec/pixel. The filters were selected to be free from polyaromatic hydrocarbon (PAH) features: a filter centred at 11.88  $\mu\text{m}$  and with half bandwidth of 0.37  $\mu\text{m}$ , and a second one centred at 18.72  $\mu\text{m}$  and half bandwidth of 0.88  $\mu\text{m}$  were used. In most cases the nodding direction was taken perpendicular to the chopping direction, keeping the four resulting beams inside the VISIR field of view, which effectively limits the total field of view to  $\sim 9 \times 9$  arcsec. Identical distances, typically 8 or 10 arcsec, were used for nodding and chopping. A few galaxies, which were known *a priori* to harbour extended emission – star-forming clusters or rings – were observed in parallel nodding mode, providing a field of view of  $19.2 \times 19.2$  arcsec. Each science observation was immediately followed by a standard star, which was used for both photometric calibration and for point spread function (PSF) control. The accuracy of the absolute flux calibration is limited by the uncertainties in the flux calibration of the mid-IR standard stars and is estimated to be  $\sim 10\%$ . Errors given in the later sections and tables are statistical.

Data reduction was done with the ESO pipeline, which was further modified by us to remove the striping pattern of the detector and to improve the centring of the chopped frames. Using service mode for the observations guaranteed both reaching the diffraction limit and acceptable levels for striping. As the intensity of striping depends roughly on the brightness of the sky and its variability, observations with strong striping were rejected by the telescope staff and repeated at a later time. Low-level striping was easy to remove by fitting and subtracting a low-order polynomial along image rows with suitable pixel rejection criteria to guarantee that the observed galaxy or star is not included in the fit.

The data reduction procedure consists of simply shifting and stacking chopped/nodded frames. To provide the most accurate combination of frames for bright sources, the shortest individual exposures at each chopping position – typically an integration time of a few seconds – were combined by using centroiding on the source itself (marked with a \* in Table 3). For fainter sources centroiding was done on the combined nodding/chopping exposure – typically representing around 1 minute of integration time (marked with a \*\* in Table 3). A few sources are too faint at 11.8  $\mu\text{m}$  for any centroiding and we were forced to rely on telescope guiding for combining each beam. This is typically also the case at 18.7  $\mu\text{m}$ . The same combination scheme was always used for both the galaxy and its associated PSF standard. Finally, the four beams were combined.

The accuracy of the absolute flux calibration is limited by the uncertainties in the flux calibration of the mid-IR standard stars and is estimated to be 5 - 10%. Flux errors given in the tables are statistical. When available, we compared our VISIR photometry with equivalent measurements reported in the literature. The agreement is in general good within the errors, but some discrepancies exist. The result of this comparison is discussed on a case basis at each object section.

## 3 ANALYSIS

### 3.1 Quality of the PSF

The full width at half maximum (FWHM) resolution achieved in the standard star images is typically 0.31–0.35 arcsec at 11.8  $\mu\text{m}$  and 0.49–0.53 arcsec at 18.7  $\mu\text{m}$  (Table 2). The observations of the PSF stars often show an elongation, predominantly along the nodding direction. The reason for the elongation is unclear: Tokovinin, Sarazin & Smette (2007) suggests that it may be related to the tilt anisoplanatism between the guide star and the object. The direction of elongation does not depend on the rotation angle of the instrument and is therefore not caused by the support structure of the secondary mirror. Table 2 gives the residual ellipticity of the images  $e = 0.10 - 0.24$  at 11.8  $\mu\text{m}$  ( $e = 0.15$  on average) and slightly lower  $e = 0.03 - 0.15$  ( $e = 0.10$  on average) at 18.7  $\mu\text{m}$ .

In order to investigate this intrinsic, variable elongation and its effect on the analysis of the science data further, an average of all standard star observations was taken and subtracted this from the individual standard star observation. A typical residual was a pair of central symmetric lobes with varying position angle (Fig. 1). The same residual is often

**Table 1.** The AGN sample observed with VISIR. The distance,  $D$ , was derived from the velocity  $v_{3K}$  provided in NED, except for NGC 1386, NGC 5128 and Circinus, which are from Madore et al. (1999), Ferrarese et al. (2007) and Freeman et al. (1977), respectively. Galaxy morphology and classification are from NED. The 12 and 25  $\mu\text{m}$  IRAS fluxes are from (Moshir et al. 1990). The last two columns give total on-source integration time.

Galaxy	$z$	$D$ Mpc	Scale pc/arcsec	Host type	AGN	12 $\mu\text{m}$ Jy	25 $\mu\text{m}$ Jy	$t_{11.8}$ s	$t_{18.7}$ s	Observing date	
										11.8	18.7
NGC 1097	0.004240	15.1	73	SBb	Sy1	1.985	5.509	660	1000	2006-09-04	2006-09-05
NGC 1386	0.002895	18.6	90	SB0	Sy2	0.493	1.433	600	1000	2006-08-17	2006-08-16
NGC 1566	0.005017	20.5	99	SABbc	Sy1	0.831	1.219	600	1120	2006-09-05	2006-09-05
ESO 434-G040	0.008486	39.2	190	SA0	Sy2			600	1800	2006-04-28	2005-12-18 2006-03-13
Mrk 1239	0.019927	86.6	420	E-S0	Sy1.5	0.65	1.141	600	1000	2006-04-28	2006-05-16
NGC 3783	0.009730	44.3	215	SBa	Sy1	0.840	2.492	600	600	2006-04-29	2006-03-13
M87	0.004360	22.4	109	E0-1 pec	Sy	0.231	<0.25	3560	1870	2006-03-09	2006-03-09 2006-05-17
Sombbrero	0.003416	18.7	91	SAa	Sy1.9	0.386	0.497	800	...	2006-03-22	...
NGC 5128	0.001825	3.4	17	S0 pec	Sy2	13.26	17.26	300	750	2006-03-15	2006-03-22
NGC 5506	0.006181	29.0	141	Sa pec	Sy1.9	1.282	3.638	600	1000	2006-06-06	2006-06-06
Circinus	0.001448	4.2	20	SAB	Sy2	18.8	68.44	500	1000	2006-06-05	2006-03-27
NGC 7469	0.016317	61.9	300	SABa	Sy1.2	1.348	5.789	600	1020	2006-07-14	2006-08-06
NGC 7582	0.005254	18.3	89	SBab	Sy2	1.620	6.436	750	1000	2006-08-06	2006-06-16

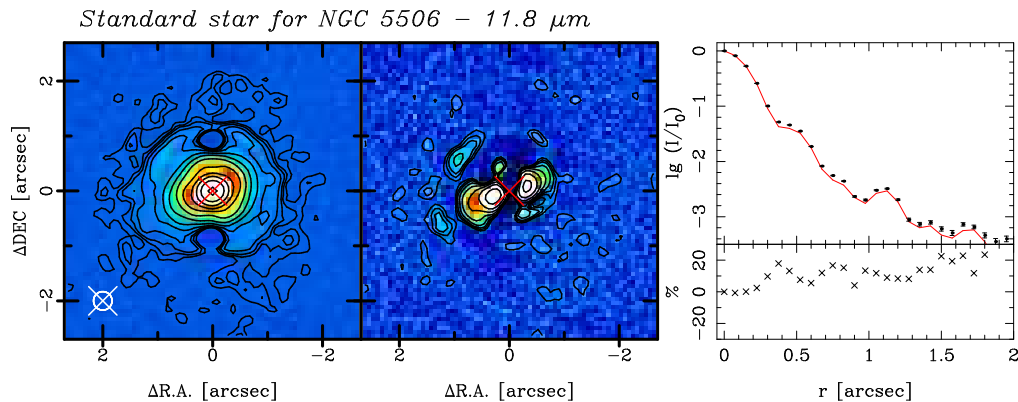


**Figure 1.** The 11.8  $\mu\text{m}$  PSF standard of NGC 5506. *Left:* observed emission. *Middle:* the residual after subtracting the average PSF. *upper Right:* radial profiles in logarithmic flux units normalized at  $r = 0$  for the standard star plotted with errorbars and the average PSF standard (redline). The circle on the lower left corner notes the FWHM size, while the size of the cross at the nucleus indicates the size of the first diffraction ring ( $1.22\lambda D^{-1}$ ). *Lower right* the residual (observed - average PSF) in %s is shown. North is up, and east is to the left, and the distances are given in arcseconds. The lowest contours are at a 3, 5, 7, 11, 19 level.  $1\sigma$  is 23 mJy arcsec $^{-2}$ .

present when comparing the galaxy observation with its associated PSF star (e.g. Fig. 8) and is therefore taken to be an artefact in the present analysis.

The FWHM of the PSF stars is rather stable and similar to that measured at the galaxies nucleus. The standard deviation of the FWHM measurements in the PSF star frames is  $\sigma = 0.014$  arcsec at 11.8  $\mu\text{m}$  and  $\sigma = 0.013$  arcsec at 18.7  $\mu\text{m}$ . In two cases the nucleus FWHM is significantly higher than that of the corresponding PSF star, both in the 18.7  $\mu\text{m}$  images: NGC 7582, where the extended emission from the star-forming ring affects the measurement of the core width, and NGC 1386, which presents the strongest extended nuclear emission in the sample.

### 3.2 Extended emission

In all cases, the most conspicuous source at these wavelengths is the nucleus. The detection of low surface bright-

ness emission around the nucleus is limited by the chopping technique used in ground mid-IR observations. Nevertheless, in some cases extended nuclear emission and circumnuclear star-forming regions are strong enough to be detected. To search for extended emission, both a PSF-subtraction and a radial profile analysis were used. In the first case, the PSF star was subtracted from its associated-in-time galaxy observation after normalizing it to the galaxy peak at the nucleus. The residual map thus has zero flux at the very centre, and possible differences in the shapes of the PSF star and galaxy are then visible as negative or positive fluxes. In some cases, these residuals take the form of two symmetric central blobs and should be ignored (see Sect. 3.1). In addition, radial profiles were extracted by azimuthally averaging the emission about the nucleus. This analysis is more sensitive to the presence of extended emission due to the accumulated higher S/N and is also less affected by PSF variations.

Therefore radial profiles are used as primary indicators for the presence of extended emission.

### 3.3 Nuclear photometry

Nuclear point-like fluxes were derived from both the radial profile analysis and direct aperture photometry (Table 3). In cases where the emission is clearly extended, a nuclear point-like flux (Table 3) is derived from a fit to the radial profile. The fit has two components: a disc profile ( $I = I_0 \exp^{-r/r_0}$ ) convolved with the associated PSF star representing the extended component, and the profile of the PSF star representing the unresolved nucleus. For some galaxies, the associated PSF star was too faint at the wing levels. In that case, a combined PSF profile was created by replacing the region beyond  $\sim 1$  arcsec with the profile of the brightest PSF star in the sample, HD 2261 (35 Jy at  $11.8 \mu\text{m}$  and 15 Jy at  $18.7 \mu\text{m}$ ).

In galaxies with weak extended emission, nuclear aperture photometry was used instead. The optimal aperture radius was determined by comparing the galaxy radial profile with that of the PSF star. The radius at which the galaxy radial profile began to diverge from that of the PSF was selected and a core flux derived. The point-like flux in Table 3 is the core value multiplied by a correction factor – to account for the additional unresolved nuclear flux contained in the PSF wings.

Finally, in pure unresolved nuclear sources, fluxes are directly those measured in an aperture containing all the observed emission. We note, however, that in these cases emission from the nuclear PSF wings is weak or undetected. Following the same procedure as before, a correction factor – derived from the PSF star radial profile – to account for the additional flux in the nuclear PSF wings was applied to the total observed emission and this is given in the point-like flux column in Table 3. It can be seen from the comparison between the observed flux and the point-like flux that this correction factor is small, between  $< 5$  to 10% on average.

## 4 DESCRIPTION OF GALAXIES

Figures 2, 5, 6, 7, 8 and 10 present VLT-VISIR 11.8 and  $18.7 \mu\text{m}$  images for the sample galaxies. For each image, there is a residual map after a PSF star subtraction and a radial profile analysis. Only the central  $5 \times 5$  arcsec<sup>2</sup> region is shown, as no emission is detected further out except in the case of NGC 1097 (Fig. 3). In all cases, the lowest contour level displayed is  $3\sigma$ .

A brief description of the results for each galaxy is provided in following sections. The VISIR nuclear fluxes are compared with the large-aperture satellite measurements generally used at these mid-IR wavelengths. *IRAS* 12 and  $25 \mu\text{m}$  are taken as a reference. The *IRAS* 12  $\mu\text{m}$  bandpass is  $8.5\text{--}15 \mu\text{m}$  and the *IRAS* 25  $\mu\text{m}$  bandpass is  $19\text{--}30 \mu\text{m}$ . These bands include the silicate absorption feature, several PAH features and emission lines. On the other hand, the VISIR filters are narrow-band and mostly line-free. The comparison illustrates the difference between large-aperture satellite and current inferred AGN fluxes on scales of FWHM  $< \sim 0.5$  arcsec resolution.

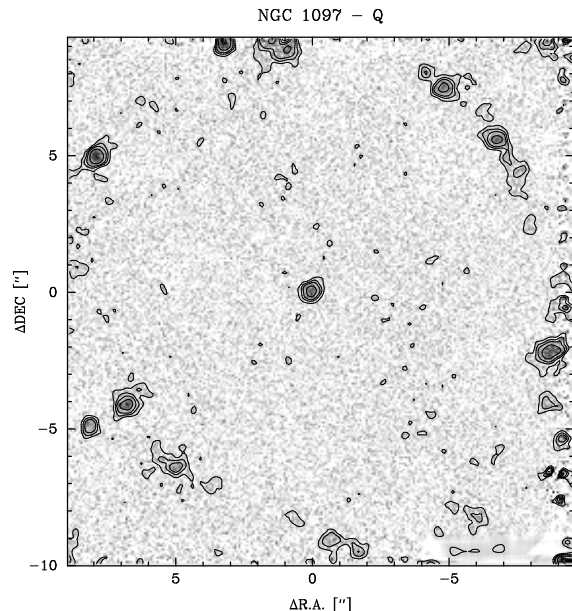


**Figure 3.** Wide-field VISIR  $18.7 \mu\text{m}$  image of NGC 1097 showing the kpc-radius star-forming ring. Up to more than 12 clumps are isolated in this image above the 3 sigma level (first contour in the image).  $1 \sigma$  is  $16 \text{ mJy arcsec}^{-2}$

### 4.1 NGC 1097

NGC 1097 has a LINER/Seyfert 1 nucleus surrounded by a star-forming ring of radius  $r \simeq 8$  arcsec or  $\sim 600$  pc. In the  $2\text{--}4.5 \mu\text{m}$  range, the nuclear region is unresolved down to scales of FWHM  $< 10$  pc from adaptive optics VLT/NaCo images (Prieto, Maciejewski & Reunanen 2005).

Figure 2 shows the central  $5 \times 5$  arcsec<sup>2</sup> region in the  $11.8$  and  $18.7 \mu\text{m}$  VISIR images. The most prominent feature is the nucleus, unresolved at the achieved spatial resolution: FWHM  $< 30$  pc. The residual images after the subtraction of the associated PSF star do not reveal any extended nuclear emission and the radial profiles show that both the nucleus and the PSF star profiles agree to within the errors. The complete VISIR field of view at  $18.7 \mu\text{m}$  (Fig. 3) is one of the deepest images of the starforming ring and nucleus of this galaxy at this wavelength, presenting more than 12 starforming knots in the ring. The VISIR  $11.8 \mu\text{m}$  image is worse in quality, due to a high background residual, and only three regions of the ring are detected. More star forming regions at this wavelength are detected by Mason et al. (2007) using Gemini/T-ReCS.

The nuclear fluxes reported by Mason et al. (2007) in a  $1.5$  arcsec aperture radius are larger by a factor 2 at  $11 \mu\text{m}$  and a factor 1.5 at  $18 \mu\text{m}$  than those found by us, either after integrating in an aperture containing all the observed emission or from the radial profile analysis (Table 3). The reason for this difference is not clear. Mason’s et al filters are much broader than the ones used by us (their filters are  $18.3 \mu\text{m}$  filter with half bandwidth =  $1.51 \mu\text{m}$  and  $11.7 \mu\text{m}$  filter with  $1.13 \mu\text{m}$  half bandwidth). Accordingly, their  $11.7 \mu\text{m}$  may include the contribution of the usually strong  $11.2 \mu\text{m}$  PAH feature. However, the results from IR nuclear spectroscopy carried by the same authors indicate the absence of other PAH features in the nucleus of NGC 1097. Thus, the

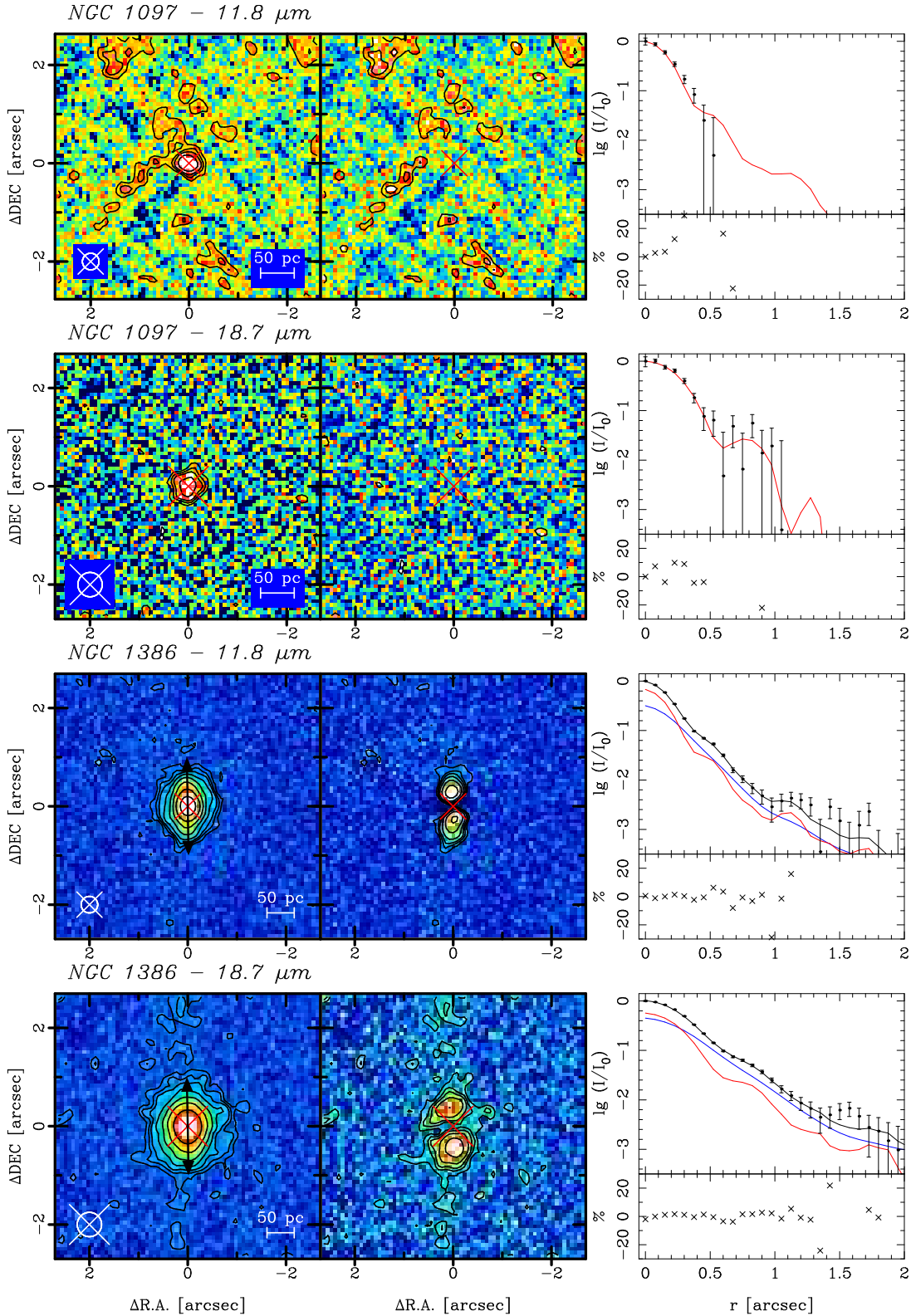


**Figure 2.** The 11.8 and 18.7  $\mu\text{m}$  images for NGC 1097 and NGC 1386. North is up, and east is to the left. *Left:* observed emission, the circle on the left corner represents the PSF FWHM, the size of the cross at the nucleus indicates the size of the first diffraction ring ( $1.22\lambda D^{-1}$ ). The location of the ionization cone in NGC 1386 is indicated by an arrow. The 11.8  $\mu\text{m}$  map of NGC 1097 suffers from poor sky subtraction. *Middle:* residual after PSF subtraction. *Upper right:* radial profiles in logarithmic flux units normalised at  $r = 0$  for the galaxy plotted with errorbars, the PSF standard (red line), fitted disk component (blue line) and the combined model (black line). *Lower right:* the residual (observed - model) in percent is shown. Contours are at  $3\sigma$ , 5, 7, 11, 19 levels;  $1\sigma$  in NGC 1097 is 29 mJy arcsec $^{-2}$  at 11.8  $\mu\text{m}$ , 16 mJy arcsec $^{-2}$  at 18.7  $\mu\text{m}$ ; in NGC 1386 is 19 mJy arcsec $^{-2}$  at 11.8  $\mu\text{m}$ , 33 mJy arcsec $^{-2}$  at 18.7  $\mu\text{m}$ .

**Table 2.** FWHM, ellipticity  $e$  and position angle (PA) for the standard star observations and galaxies. The measurements marked with \* and \*\* are produced by using centroiding for exposure with an integration time of a few seconds (\*) or around one minute (\*\*); see Section 2 for details.

Object	HD	PSF star observations						Galaxy observations					
		11.8 $\mu\text{m}$		18.7 $\mu\text{m}$		11.8 $\mu\text{m}$		18.7 $\mu\text{m}$					
		FWHM	$e$	PA	FWHM	$e$	PA	FWHM	$e$	PA	FWHM	$e$	PA
"	"	°	"	"	°	"	"	°	"	"	°		
NGC 1097	16815	0.35	0.10	-86	0.50	0.15	-82	0.37	0.13	3	0.54	...	-9
NGC 1386	26967	0.33*	0.21	-80	0.53	0.08	-70	0.36*	0.27	1	0.58	0.28	-2
NGC 1566	26967	0.34	0.19	-79	0.49	0.03	6	0.32	0.38	-75	0.50	0.56	16
ESO 434-G040	75691	0.31*	0.11	87	0.48	0.10	-79	0.31*	0.10	-83	0.50	0.28	-63
	75691	...	...	...	0.50	0.05	-79	...	...	...	0.51	0.06	40
Mrk 1239	83425	0.33	0.15	-83	0.49	0.09	-69	0.32	0.09	-79	0.49	0.12	-83
NGC 3783	102964	0.31*	0.17	-80	0.50	0.08	85	0.32*	0.02	82	0.50	0.15	-13
M87	108985	0.31	0.10	-81	...	...	...	0.35	0.55	-90	...	...	...
	108985	0.32	0.11	89	...	...	...	0.28	0.72	-2	...	...	...
NGC 5128	119193	0.31*	0.11	-71	0.51**	0.45	-82	0.31*	0.05	-76	0.52**	0.11	47
NGC 5506	124294	0.32*	0.24	-78	0.49**	0.15	-83	0.33*	0.26	86	0.52**	0.22	89
Circinus	128068	0.35*	0.14	-67	0.50**	0.08	-78	0.36*	0.11	-44	0.51**	0.17	-77
NGC 7469	5112	0.32*	0.17	86	0.49	0.14	80	0.33*	0.51	-74	0.51	0.10	33
NGC 7582	2261	0.33	0.11	83	0.49	0.12	-87	0.33	0.06	-45	0.70	0.27	-11

**Table 3.** Photometry: columns #2 and #3 are integrated fluxes in a radius  $r$ , in brackets; errors refer to background noise; #4 is an upper limit to the nuclear size; #5 and #6 are nuclear point-like source fluxes, values marked with  $^f$  are inferred from the fitting analysis; all others are from aperture photometry (see Sect. 3.3); #7 & #8 are fluxes from the extended component, whose size and orientation are given in #9.

Object	Total flux in (radius $r$ )		Nucleus size	Unresolved source		Circumnuclear		Extended emission location and size at radius $r$
	11.8 $\mu\text{m}$	18.7 $\mu\text{m}$	11.8 $\mu\text{m}$	11.8 $\mu\text{m}$	18.7 $\mu\text{m}$	11.8 $\mu\text{m}$	18.7 $\mu\text{m}$	
	mJy	mJy	pc	mJy	mJy	mJy	mJy	
NGC 1097	25 $\pm$ 2(0.75)	41 $\pm$ 4(0.75)	27	26	49			>500
NGC 1386	353 $\pm$ 4(1.13)	757 $\pm$ 6(1.13)	32	195 $^f$	330 $^f$	170 $^f$	430 $^f$	stellar ring at $r \gtrsim 8''$ along ion. cone at $r \gtrsim 1''$
NGC 1566	59 $\pm$ 3(0.75)	114 $\pm$ 4(0.75)	31	63	128			
ESO 434-G040	573 $\pm$ 6(1.50)	1540 $\pm$ 7(1.13)	60	590	1450			
Mrk 1239	570 $\pm$ 4(1.13)	890 $\pm$ 10(1.13)	134	590	930			
NGC 3783	535 $\pm$ 4(1.13)	1470 $\pm$ 10(1.13)	69	520	1400		90	North at $r \lesssim 2''$ (18.7 $\mu\text{m}$ )
M87	16 $\pm$ 0.8(0.75)	$\sim$ <18 (0.75)	35	17		1.6		jet-knot at $r \sim 0''.87$ (HST1)
Sombrero	<7	...	...	...	...			
NGC 5128	1150 $\pm$ 5(1.13)	2900 $\pm$ 30(1.5)	5	1150 $^f$	2300 $^f$	30 $^f$	770 $^f$	along jet at $r < 1''$ (18.7 $\mu\text{m}$ )
NGC 5506	958 $\pm$ 5(1.5)	1990 $\pm$ 20(1.5)	47	900 $^f$	1400 $^f$	65 $^f$	590 $^f$	East to West at $r \lesssim 1''.5$
Circinus	11400(2.63)	24700(2.63)	7	9300 $^f$	17600 $^f$	2100 $^f$	7400 $^f$	along ion. cone at $r \lesssim 2''.5$
NGC 7469	917 $\pm$ 8(2.25)	2470 $\pm$ 20(2.25)	99	530	1270	390	1200	stellar-ring at $1'' < r < 2''.5$
NGC 7582	943 $\pm$ 7(2.63)	1880 $\pm$ 20(2.63)	29	405	550	540	1330	stellar-ring at $0''.5 < r < 2''$

plausible explanation for the difference is genuine nuclear variability, by a factor of 2 or so in a time scale of 1 year, the spanning time between both observation sets.

Comparing with large aperture *IRAS* (Table 1) or *Spitzer* (6.6 Jy at 24  $\mu\text{m}$ ; Dale et al. 2007) fluxes, they are two orders of magnitudes larger than the nuclear fluxes reported here. In this case, the IR satellite fluxes are dominated by the prominent star-forming ring of NGC 1097. The observed 18.7  $\mu\text{m}$  flux in the ring is  $\gtrsim$  500 mJy (no reliable estimate is possible at 11.8  $\mu\text{m}$ ). This is a lower limit due to the observational limitation of chopping; also the full extension of the ring is not included within the VISIR field of view. Still this lower limit is already an order of magnitude higher than that of the AGN, indicating that at mid-IR wavelengths star formation and not the AGN is the dominant contributor. This is full in line with the result derived from the analysis of the spectral energy distribution of this

nucleus based on very high resolution data, from UV to optical to IR. This study shows that the genuine AGN luminosity in NGC 1097 is indeed a tiny fraction, less than 1%, of the total IR luminosity integrated over the galaxy (Prieto et al. 2009).

## 4.2 NGC 1386

NGC 1386 is an inclined, barred lenticular galaxy with a Seyfert 2 nucleus. The nuclear region is crossed by dust lanes, which are preferentially distributed along the galaxy major axis at PA $\sim$ 20°. The [O III] 5007 Å emission is highly collimated and extends along the same direction, north-to-south, up to  $\sim$ 3 arcsec radius from the center (Schmitt et al. 2003; Fig. 2).

Both 11.8 and 18.7  $\mu\text{m}$  VISIR images also show elongation along the north–south direction but up to  $\sim$ 1 arcsec

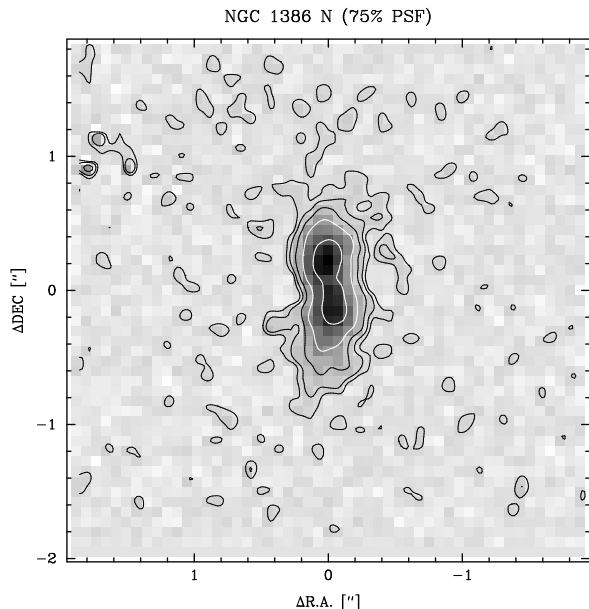


**Figure 4.** The 11.8  $\mu\text{m}$  emission of NGC 1386 with the PSF scaled to 75% of the peak flux of the nucleus and subtracted. The contours are placed at logarithmic intervals at 1.5, 3, 6, 12 and  $24\sigma$ .

from the centre (Fig. 2). Although the elongation is in the direction of telescope chopping and could be caused by this, we tend to believe that it is real as it is present at both wavelengths, covering a similar size. None of the PSF star observations in either band show similar structure (see table 2). Also, the symmetric double-lobe residual seen after subtracting the PSF (Fig. 2) remains the same even if the PSF is rotated by 90 degrees. As north–south is a preferential emission direction in this galaxy we consider the extension to be genuine. The radial profiles at both wavelengths (Fig. 2) are similar, presenting excess emission up to even larger distances of 1.5–2.0 arcsec. Figure 4 shows a residual image at 11.8  $\mu\text{m}$  after scaling the PSF star to 75% of the galaxy peak. The scale factor is chosen to minimize negative fluxes seen when scaling to 100 % of the peak (Fig. 2). The resulting morphology is now smoother and continuous, in line with that seen in the [O III] line emission.

The total integrated flux at 11.8  $\mu\text{m}$  is 15% difference from that reported by Siebenmorgen, Krügel & Spoon (2004) using ESO-3.6m / TIMMI2 with a much broader filter centered at 11.9  $\mu\text{m}$  (FWHM = 2.26  $\mu\text{m}$ ). Since this filter includes the strong PAH feature at 11.2  $\mu\text{m}$ , the flux difference can partially be attributed to this contribution and the photometry errors.

The results from the profile fitting analysis further indicate that the contribution of the unresolved source (the AGN) is  $\sim 50\%$  of the total measured at each of the wavelengths, with the other half being associated with the north-south extended emission. Comparing with the large aperture *IRAS* data, the inferred AGN contribution is again much less,  $\sim 40\%$  of the *IRAS* 12  $\mu\text{m}$  and  $\sim 20\%$  of the *IRAS* 25  $\mu\text{m}$  flux levels. It can be readily seen that the difference with the *IRAS* 12  $\mu\text{m}$  flux is the contribution of the extended nuclear emission seen by VISIR. This is not the case at 25  $\mu\text{m}$ , and thus most of the emission at this wavelength must

come, plausibly, from a more diffuse extended emission over the galaxy.

### 4.3 NGC 1566

NGC 1566 is a face-on spiral galaxy with a Seyfert 1 nucleus. The nucleus is known to be variable from X-rays to IR (Baribaud et al. 1992; Glass 2004). At near-IR wavelengths, 1–4  $\mu\text{m}$  adaptive optic images, the nucleus is unresolved down to scales of FWHM < 11 pc at 2  $\mu\text{m}$  (Prieto et al. 2007, 2009). The *HST* [O III] images show a one-sided ionization cone towards the south-west direction (Schmitt & Kinney 1996).

The VISIR images (Fig. 5) at both wavelengths just reveal a dominant central unresolved source with size FWHM < 31 pc at 11.8  $\mu\text{m}$ . The [*IRAS* 12  $\mu\text{m}$  and ISOCAM 8.5–10.7  $\mu\text{m}$  fluxes (Ramos Almeida et al. 2007) are larger, by factors of 13 and 4 respectively, than the 11.8  $\mu\text{m}$  nuclear flux reported here. The *IRAS* 25  $\mu\text{m}$  flux is a factor 10 higher than the 18.7  $\mu\text{m}$  flux. The smaller difference with Ramos et al. is because of the deconvolution procedure applied to the ISOCAM radial light profile, which helps reducing the galaxy contribution, but obviously is insufficient to overcome the poor ISO spatial resolution. Thus, most of the emission measured in this object in IR large aperture data is dominated from other sources in the galaxy, and the AGN contribution to the total is minor. The analysis of the SED of this nucleus based on very high resolution data from UV to optical to IR shows that indeed that is the case: the intrinsic AGN luminosity is two orders of magnitude lower than that of the galaxy (Prieto et al. 2009).

### 4.4 ESO 434-G040

ESO 434-G040 (MCG-05-23-016) is an SA galaxy with a Seyfert 2 nucleus but with broad Paschen and Brackett series H II lines (Veilleux, Goodrich, & Hill 1997). A dust lane crosses the nuclear region on its south-eastern side, at a distance of less than 1 arcsec from the centre. The [O III] gas emission extends in the north-east–south-west direction by 1 arcsec (Ferruit, Wilson, & Mulchaey 2000), as shown in Fig. 5.

The VISIR images are dominated by a bright point-like source (Fig. 5). The structure seen in the residual image at 11.8  $\mu\text{m}$  is an artefact (sect 3.1); the nature of the residuals at the 18.7  $\mu\text{m}$  image is uncertain, however, there is marginal excess emission in the 18.7  $\mu\text{m}$  radial profile ( $\sim 190$  mJy, see Table 3). No reported *IRAS* measurements were found.

### 4.5 Mrk 1239

Mrk 1239 is an elliptical / S0-class galaxy with a Seyfert 1.5 nucleus. It is the most distant object in the sample, 20 times the distance to Circinus (Table 1).

VLT/MIDI interferometric observations in the 8–12  $\mu\text{m}$  range are consistent with an unresolved nucleus (Tristram 2009). VLT/NACO adaptive optic images in the 1–4  $\mu\text{m}$  range set an upper limit for the unresolved nucleus down to scales of FWHM < 38 pc at 2  $\mu\text{m}$  (Prieto et al. 2009). VISIR 11.8 and 18.7  $\mu\text{m}$  images are also dominated by an unresolved central source with no extended emission detected in

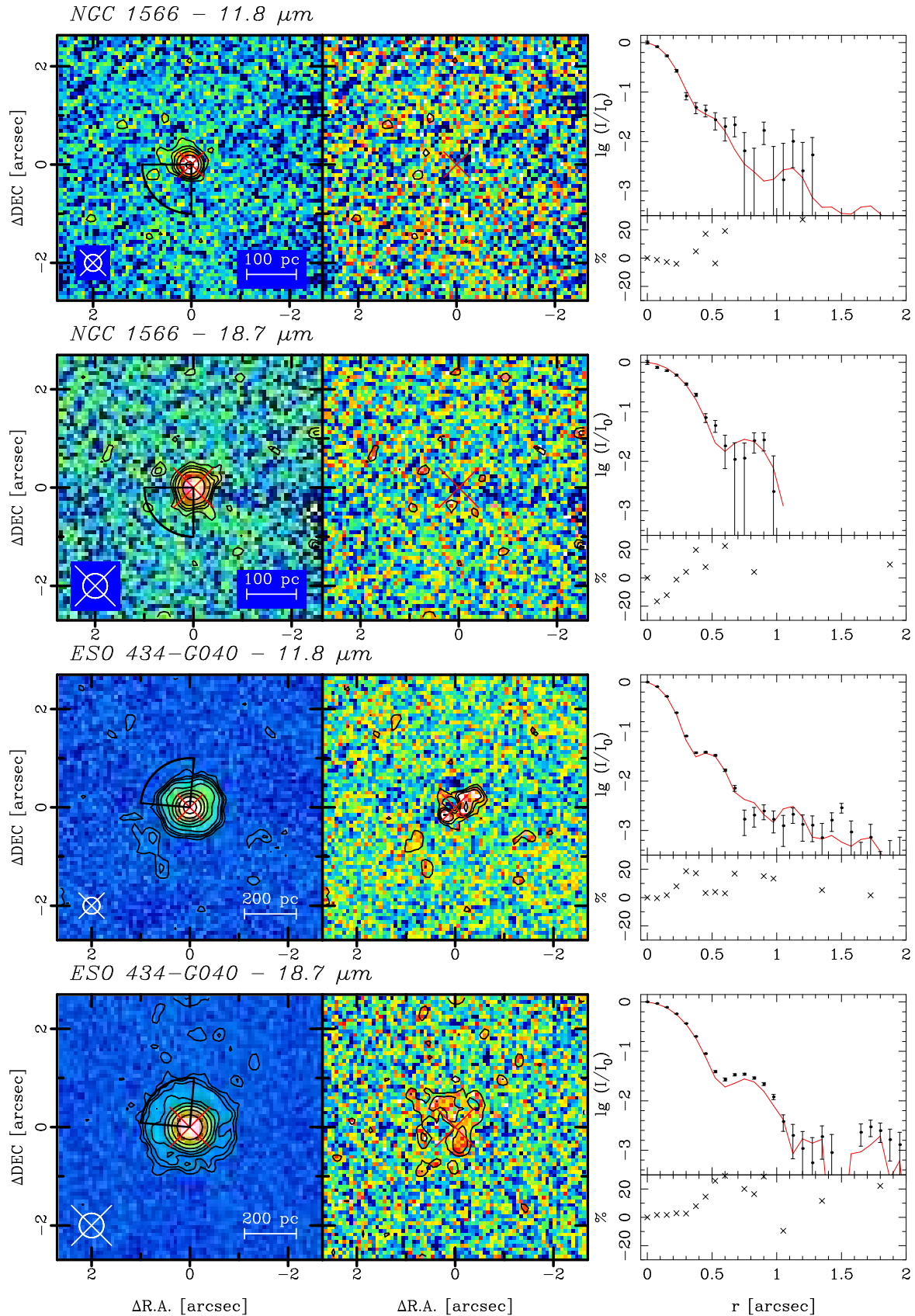


**Figure 5.** As in Fig. 2 but for NGC 1566 and ESO434-G40. The location of the respective ionised-gas cones is outlined in the figures.  $1\sigma$  level is 22 mJy arcsec $^{-2}$  at 11.8, 42 mJy arcsec $^{-2}$  at 18.7  $\mu\text{m}$ , for NGC 1566; 32 mJy arcsec $^{-2}$  at 11.8, 55 mJy arcsec $^{-2}$  at 18.7  $\mu\text{m}$ , for ESO 434-G040.



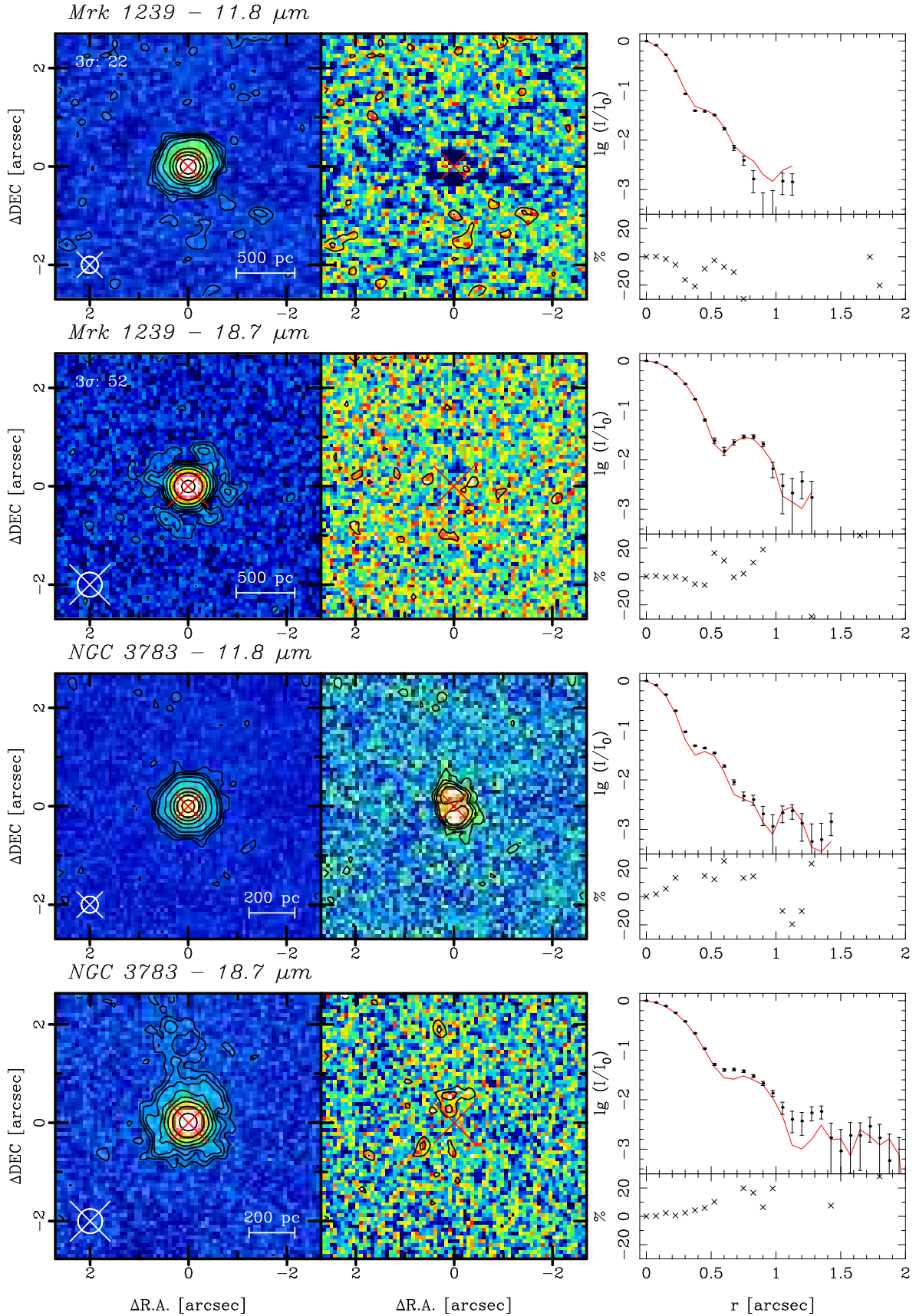


Figure 6. As in Fig. 2 but for Mrk 1239 and NGC 3783.  $1\sigma$  level is 23 mJy arcsec $^{-2}$  at 11.8, 55 mJy arcsec $^{-2}$  at 18.7  $\mu\text{m}$ , for Mrk 1239; 23 mJy arcsec $^{-2}$  at 11.8, 70 mJy arcsec $^{-2}$  at 18.7  $\mu\text{m}$ , for NGC 3783.

either the residuals or the radial profile analysis (Fig. 6). The extended optical ionised gas in this galaxy shows neither a particular morphology, it extends around the nucleus up to about 8 arcsec radius (Mulchaey, Wilson & Tsvetanov, 1996).

Our photometry at 11.8  $\mu\text{m}$  is in excellent agreement, 5% difference, with that reported by Maiolino et al. (1995), who observed with a 5.3 arcsec-aperture bolometer at the TMT using a N-broad-band filter centered at 10.6  $\mu\text{m}$ . The agreement indicates that this nucleus is not variable on scales of at least 11 years, and that not active star formation is occurring nucleus, otherwise emission from PAH features should have made a difference at the N-band filter observations.

Mrk 1239 is one of the three galaxies in the sample – the other cases are NGC 5506 and NGC 3783 – where the AGN accounts for almost all of the IR emission measured in the entire galaxy: the VISIR fluxes are 80 to 90 % of the *IRAS* fluxes at 12 and 25  $\mu\text{m}$  respectively (Tables 1 and 3).

#### 4.6 NGC 3783

NGC 3783 is a nearly face-on spiral galaxy with a Seyfert 1 nucleus. The [O III] emission extends over a surrounding halo up to 200 pc from the centre (Schmitt et al. 2003); higher-ionization coronal gas ([Fe VII], [Fe X]) extends further up to 400 pc from the nucleus in the north–south direction (Rodríguez-Ardila et al. 2006).

From VLT/NACO adaptive optics images in the 1–4  $\mu\text{m}$  range, the nucleus is unresolved down to scales of FWHM < 22 pc at 2  $\mu\text{m}$  (Prieto et al. 2007, 2009). But first VLTI/MIDI interferometry results in the 8–12  $\mu\text{m}$  range point to a resolved nuclear structure with size of  $\sim$ 60–70 mas,  $\sim$ 15 pc size (Beckert et al. 2008). However this result requires further confirmation with other base-line observations.

VISIR 11.8 and 18.7  $\mu\text{m}$  images are dominated by a central bright source (Fig. 6). The central two-blob structure in the 11.8  $\mu\text{m}$  residual image is due to PSF mismatch (see Sect. 3.1). The radial profile at both wavelengths shows some marginal excess emission but that may still be introduced by slight variations in the PSF star profile. We consider the VISIR emission unresolved at the S/N limit of these observations, setting an upper limit for the nucleus size of FWHM < 68 pc at 11  $\mu\text{m}$  (Table 2).

Our photometry at 11.8  $\mu\text{m}$  differs by 20 % with respect to the value reported by Haas et al. (2007), using also VISIR but a narrow-band filter just centered on the PAH feature at 11.2  $\mu\text{m}$  (FWHM = 0.6  $\mu\text{m}$ ). Thus, the higher flux measured by Haas et al. may be due to PAH contribution - the photometric errors in both observations are about 10 %. If that is the case, some level of starformation may be present at the nuclear region at scales of less than 70 pc - the resolution of these observations. Alternatively, the difference may be due to variability at very low level: these observations and that of Haas et al are separated by one year.

Comparing with the *IRAS* flux levels at 12 and 25  $\mu\text{m}$ , the VISIR nuclear fluxes are  $\sim$ 60% lower in either band. This is a small difference as compared with most of the objects in this sample, emphasising the dominance of this AGN over the host galaxy light. The analysis of the spectral energy distribution of this nucleus on the basis of high spatial

resolution data shows indeed that this AGN behaves like a quasar dominating the integrated light at any aperture size in the 1 to 100  $\mu\text{m}$  range (Prieto et al. 2009).

#### 4.7 M87

M87 is a giant elliptical galaxy with a LINER-type nucleus. It has a one-sided jet at PA =  $-66^\circ$  extending up to 2 kpc from the nucleus. The radio, optical, and X-ray jet has several knots of which the innermost one – HST-1 at 0.85 arcsec from the nucleus – has brightened fifty-fold in the X-rays in the period 2000–2005 (Harris et al. 2006). A sudden increase in brightness from HST-1 has also been seen in the IR in our VLT/NACO *K*-band images during the same period, reaching flux levels comparable to that of the nucleus.

M87 was observed in 2006 with VISIR. At that time, only the nucleus was bright at 11.8  $\mu\text{m}$  (Fig. 7) but barely detected at 18.7  $\mu\text{m}$ . At 11.8  $\mu\text{m}$ , a faint source ( $1.6 \pm 0.3$  mJy;  $5\sigma$ ) just coinciding with the position of HST-1 is seen at both the original and the residual images. A deeper Gemini image by Perlman et al (2001), using a broad-band filter centered at 10.8  $\mu\text{m}$  (FWHM = 5.3  $\mu\text{m}$ ) shows additional jet components at larger distances. They report on marginal nuclear excess emission up to  $r > 0.6$  arcsec from the centre. The VISIR image has slightly better spatial resolution than that by Gemini (0.32 vs. 0.46 arcsec) and so far our results on the residual image and radial profile analysis are consistent with the nucleus of M87 being point-like.

The nuclear photometry was done in an aperture radius  $r < 0.75$  arcsec (Table 3) which avoids the HST-1 region. The resulting flux at 11.8  $\mu\text{m}$  is virtually the same as that reported by Perlman et al. (2001). Considering the width of the filter used by Perlman et al. the agreement emphasises the dominance of the continuum light over any line feature, in particular PAHs, in the spectrum of M87; also the nucleus was in the same steady state in 2001 (Gemini) as in 2006 (VISIR), precisely when HST-1 was active.

M87 nucleus is detected at 18.7  $\mu\text{m}$  with VISIR but the signal is very low, the integrated flux in an aperture including all the detected emission represents 3 sigma (Table 3).

M87 was not detected in the *IRAS* 25  $\mu\text{m}$  band. At 11.8  $\mu\text{m}$ , the nuclear flux accounts for less than 7% of the flux measured in the *IRAS* 12  $\mu\text{m}$  band. Thus, most of the extra emission seen by *IRAS* has to come from low surface brightness light from the galaxy itself with a minor contribution from the jet ( $\sim$ 20 mJy is the sum of the jet knots contribution detected in Perlman et al.).

#### 4.8 The Sombrero Galaxy

The Sombrero Galaxy (NGC 4594) is a spiral with a Seyfert 1.9/LINER nucleus. The galaxy is almost edge-on and is crossed mid-plane by a distinctive dust lane.

It was undetected at 11.8  $\mu\text{m}$  and thus no observations at 18.7  $\mu\text{m}$  were attempted. A formal  $6\sigma$  upper limit for an unresolved source is 7 mJy. Bendo et al. (2006) report an 8  $\mu\text{m}$  flux of 34.4 mJy based on *Spitzer* imaging; however, such a flux level would have clearly been detected by VISIR. Thus, the mid-IR emission probed by *Spitzer* or *IRAS* has to be largely diffuse, escaping detection in ground-based observations because of the chopping technique. The AGN contribution, if any, is tiny at these wavelengths.

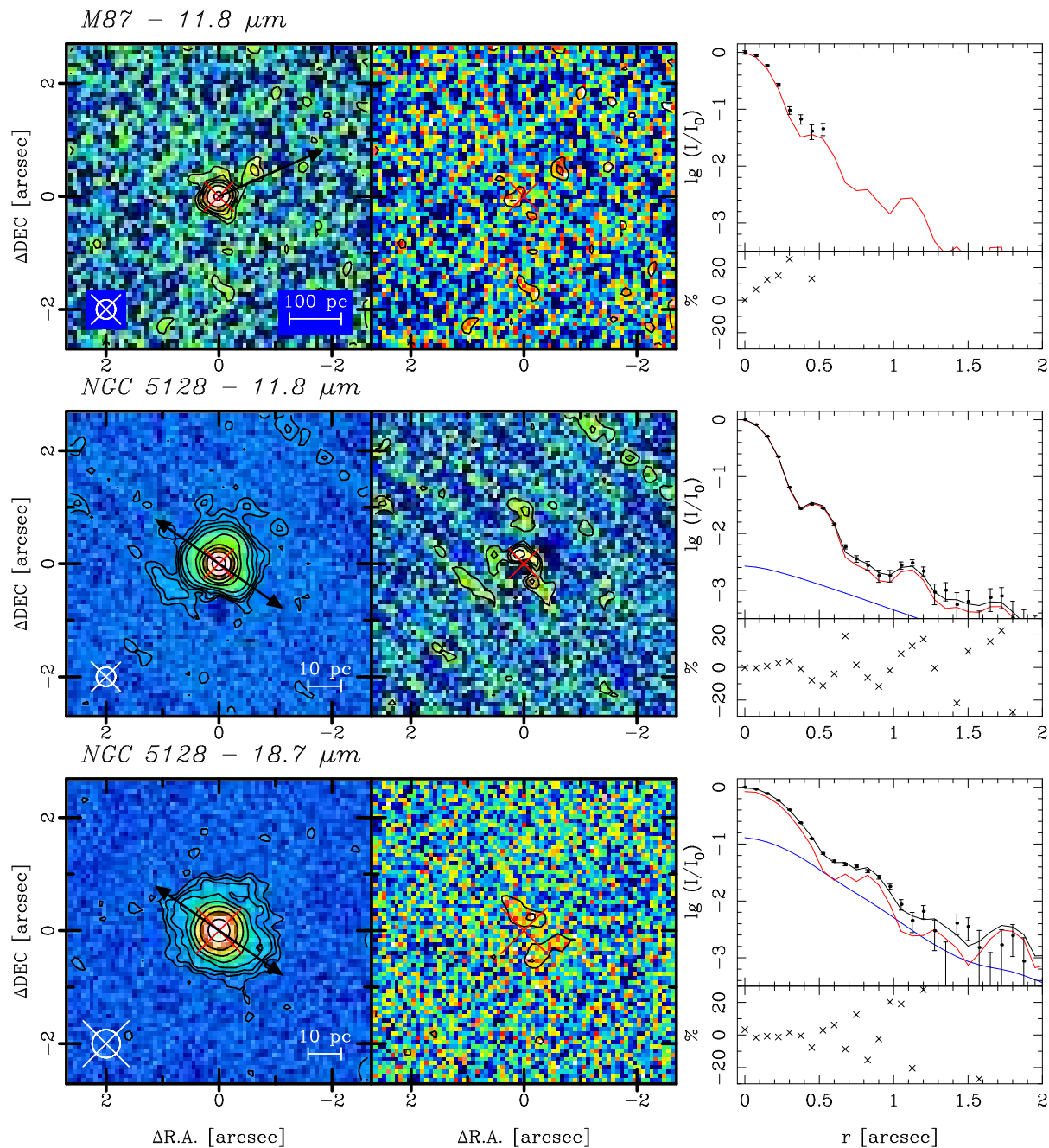


**Figure 7.** As in Fig. 2 but for M87 and NGC 5128 (Cen A). M87 is barely detected at 18.7  $\mu\text{m}$ , and it is not shown. The diagonal stripes in the 11.8  $\mu\text{m}$  image of NGC 5128 are due to sky residuals. The jet directions in M87 and NGC 5128 are indicated by an arrow in each figure.  $1\sigma$  level is 8 mJy arcsec $^{-2}$  at 11.8, 57 mJy arcsec $^{-2}$  at 18.7  $\mu\text{m}$  (not shown), for M 87; 32 mJy arcsec $^{-2}$  at 11.8, 123 mJy arcsec $^{-2}$  at 18.7  $\mu\text{m}$ , for NGC 5128.

#### 4.9 NGC 5128

NGC 5128 is the closest object in this sample. Its jet, at PA= 55 $^\circ$ , is visible from the radio to the X-ray. Adaptive optics images in the 1–5  $\mu\text{m}$  range and interferometric spectra in the 8–12  $\mu\text{m}$  range are both compatible with an unresolved nucleus down to scales of less than 1 pc (Häring-Neumayer et al. 2006; Meisenheimer et al. 2007).

The VISIR images are dominated by a bright central source (Fig. 7). At 11.8  $\mu\text{m}$  the source is rather symmetric but the radial profile reveals some marginal excess beyond

$\sim 1$  arcsec. At 18.7  $\mu\text{m}$ , the nuclear emission appears elongated in the direction of the jet. In this case, a fit to the radial profiles was attempted and the results are shown in the Figure 7. At 11.8  $\mu\text{m}$ , the fit is compatible with a single point source: the resulting point-like flux and the total integrated one are the same; at 18.7  $\mu\text{m}$ , the difference is  $\sim 20\%$ . This excess represents  $\sim 600$  mJy and presumably is from the jet. Our photometry at 11.8  $\mu\text{m}$  and 18.7  $\mu\text{m}$  differ respectively by 50% and 20% with respect to the 11.7  $\mu\text{m}$  and 17.75  $\mu\text{m}$  nuclear fluxes reported by Wysong & Antonucci

(2004). These observations were done with the Keck telescope in 2002 using filters centered at the respective wavelengths above indicated, both having a  $\text{FWHM} = 1 \mu\text{m}$ . These authors get similar spatial resolutions as the ones obtained with VISIR, and in both cases the provide flux is integration over the total detected emission. The difference in photometry is thus significant, in particular considering that no PAH features are seen in the nuclear spectrum (Siebenmorgen et al. 2004). Cen A's nucleus is the only source in Prieto's et al study (2009) whose high spatial resolution SED from radio to millimetre to IR can be fit by a single synchrotron model (Prieto et al. 2007). Thus, we believe that the fluxes difference are genuine and linked to the AGN variability.

Comparing with the large aperture *IRAS*  $12 \mu\text{m}$  and  $25 \mu\text{m}$  fluxes, the VISIR fluxes are a factor 13 and 8 smaller respectively. The analysis of the high spatial resolution SED shows indeed that the AGN represents a few percent of the total galaxy emission in the IR. Thus, most of the *IRAS* emission has to come from a source other than the AGN, presumably from a low surface brightness component.

#### 4.10 NGC 5506

NGC 5506 is an Sa galaxy with a Seyfert type 1.9 nucleus. It is orientated edge-on and crossed by dust lanes along its mid-plane, in the east-west direction. Analysis of the HST/WFPC2-F660W image shows that the  $\text{H}\alpha + [\text{NII}]$  gas extends from the center towards the north following a cone-like morphology (Fig. 8).

The nucleus, fully obscured at optical wavelengths, reveals in full realm in VLT-NACO adaptive optics images in the  $1\text{--}5 \mu\text{m}$  range. These observations set an upper limit to the core size of  $\text{FWHM} < 10 \text{ pc}$  at  $2 \mu\text{m}$  (Prieto et al. 2009).

The VISIR  $11.8 \mu\text{m}$  and  $18.7 \mu\text{m}$  images are both dominated by the nuclear source (Fig. 8). Still, there is clear extended emission, more evident at  $11.8 \mu\text{m}$ , along the east-west direction. The residual images are dominated by the symmetric two-blob structure caused by the PSF mismatch (Sect. 3.1), but some weak emission at radii larger than 1 arcsec is still apparent. The radial profiles reveal a net excess emission at both wavelengths.

A fit to the radial profiles using a composite model, a PSF star profile and a disc (Sect. 3.2), yields a dominant contribution for the point-like source at  $11.8 \mu\text{m}$ , but at  $18.7 \mu\text{m}$  the contribution of the extended emission becomes more relevant,  $\sim 30\%$  of the total flux (Table 3). Our photometry at  $11.8 \mu\text{m}$  agrees very well -  $< 5\%$  difference - with that of Siebenmorgen, Krügel & Spoon (2004), the latter obtained in 2002 with the ESO-3.6m / TIMM12 camera, The total integrated fluxes measured in both cases are compared.

At both  $11.8 \mu\text{m}$  and  $18.7 \mu\text{m}$  though, the AGN largely dominates the IR light of the entire galaxy in a similar situation as it happens in the previous described AGNs Mrk 1239 and NGC 3783: the unresolved nuclear fluxes represent 70%, at  $11.8 \mu\text{m}$ , to 40% at  $18.7 \mu\text{m}$ , of the total flux measured by *IRAS* at  $12 \mu\text{m}$  and  $25 \mu\text{m}$ , respectively. The analysis of the high-spatial-resolution spectral-energy-distribution of this nucleus shows indeed that this is another case of a Seyfert nucleus dominating the host galaxy light in a similar way as a quasar (Prieto et al. 2009).

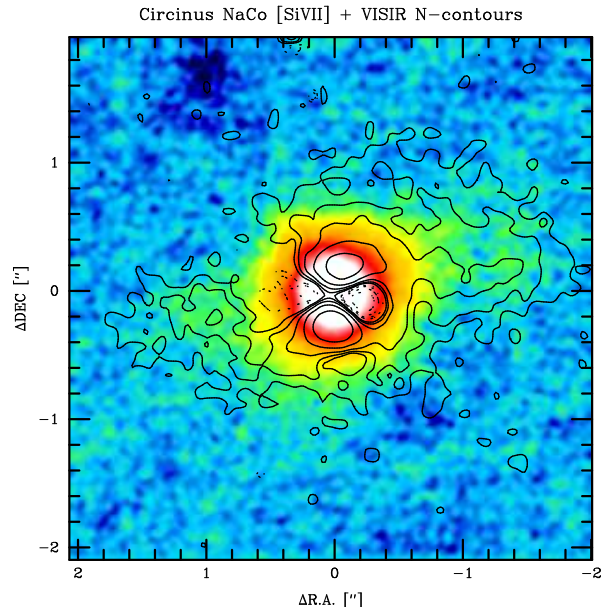


**Figure 9.** Comparison between the VLT/NaCO [SiVII]  $2.48 \mu\text{m}$  coronal line emission map (Prieto et al. 2005) and the VISIR residual image at  $11.8 \mu\text{m}$ , the latter with contours. The solid contours are at  $2.5, 5, 10, 20$  and  $40\sigma$  levels, and dotted contours indicate negative residuals. The central two-blob feature in the residual image is due to PSF mismatch, Sect. 3.1.

#### 4.11 Circinus Galaxy

The Circinus galaxy and Cen A are the two nearest AGN in this sample. Circinus is also the brightest in the IR, by an order of magnitude. Its optical ionization gas cone (Wilson et al. 2000) is seen in one direction only, northwest from the nucleus (Fig. 8); in the IR however, the high ionization coronal gas - [Si VI]  $1.96 \mu\text{m}$ , [Si VII]  $2.48 \mu\text{m}$  - reveals the counter cone location, at about the same direction as the optical ionization cone, but more collimated (Maiolino et al. 2000; Prieto, Marco & Gallimore 2005).

The nucleus of Circinus is resolved at  $2 \mu\text{m}$  with adaptive optics observations (Prieto et al. 2004; Mueller Sánchez et al. 2006). It shows a disc-like structure,  $\sim 2 \text{ pc}$  ( $\sim 0.1 \text{ arcsec}$ ) in size, oriented perpendicular to the ionization cone. The analysis of the optical-to-IR spectral energy distribution of this structure is compatible with emission by dust heated at  $\sim 300 \text{ K}$  by the AGN (Prieto et al. 2004). Further VLTI / MIDI interferometry in the  $8\text{--}12 \mu\text{m}$  range confirms this structure (Tristram et al. 2007). All the results together strongly suggests this structure to be the nuclear torus.

The VISIR images are dominated by a bright central source surrounded by a large halo ( Fig. 7). A similar morphology is seen in the Gemini/T-ReCS mid-IR images Packham et al. (2005). Within the halo, a fairly collimated light beam extends across the nucleus in the east-west direction. This is better contrasted in the  $11.8 \mu\text{m}$  residual image. The beam light is co-spatial with the also rather collimated emission defined by the [Si VII]  $2.48 \mu\text{m}$  gas traced with adaptive optics observations by Prieto et al. (2005), see Fig. 8. As this high ionization gas traces pure AGN photons, the common spatial location is an indication that the

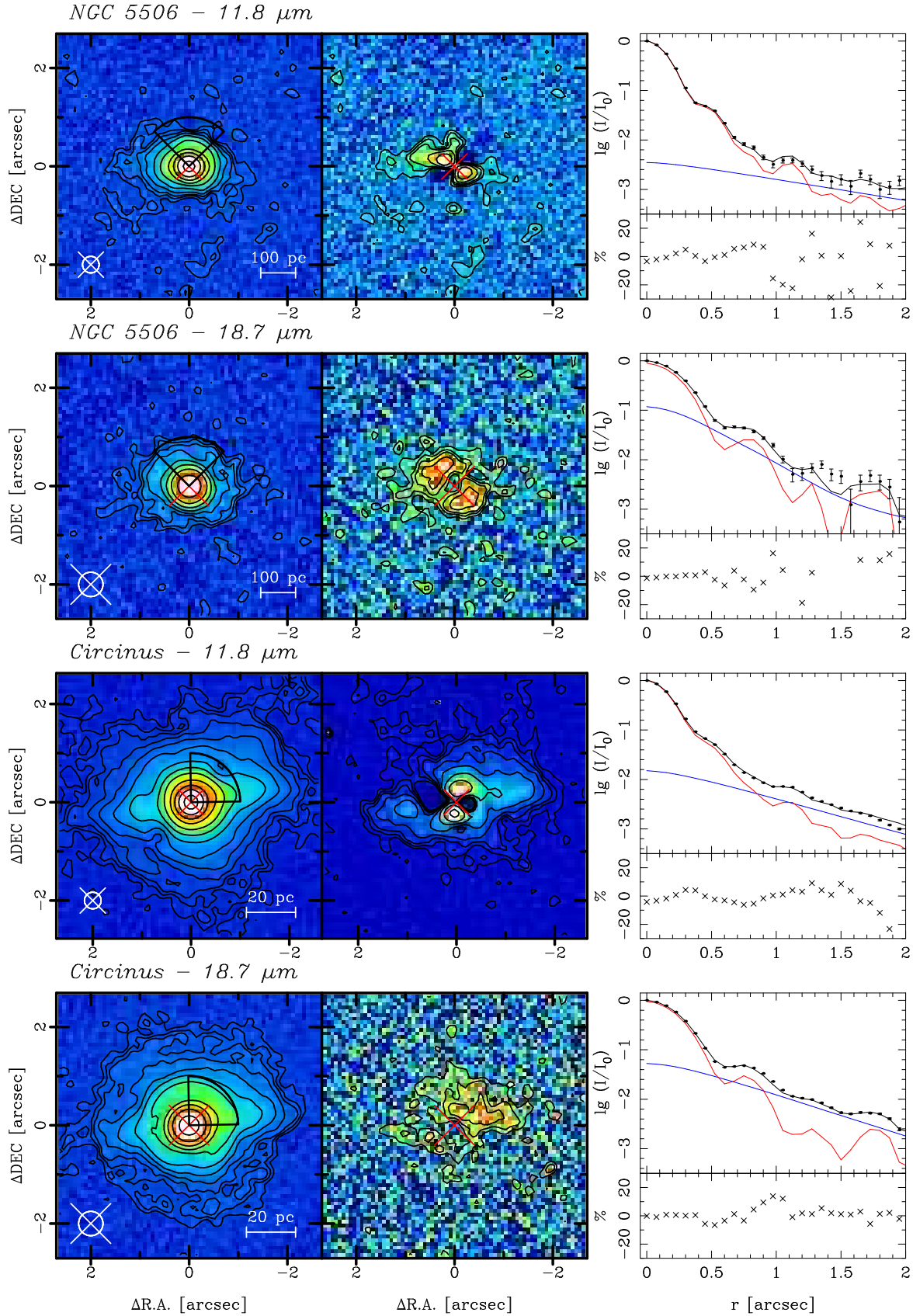


**Figure 8.** As in Fig. 2 but for NGC 5506 and Circinus. The direction and morphology of the extended ionized gas in Circinus and NGC 5506 are outlined.  $1\sigma$  level is 23 mJy arcsec<sup>-2</sup> at 11.8, 72 mJy arcsec<sup>-2</sup> at 18.7  $\mu\text{m}$ , for NGC 5506; 25 mJy arcsec<sup>-2</sup> at 11.8, 110 mJy arcsec<sup>-2</sup> at 18.7  $\mu\text{m}$ , for Circinus.



mid-IR emission is caused by dust directly heated by the AGN.

The Circinus nucleus is unresolved in the VISIR images. The achieved resolution (Table 2) corresponds to a physical scale of  $\text{FWHM} < 7$  pc at  $11.8 \mu\text{m}$ . Thus, any further extended emission from the  $\sim 2$  pc scale torus seen at  $2 \mu\text{m}$  has to extend less than  $\sim 3$  pc radius from the centre.

A composite point-like source plus disc model (Sect. 3.3) was fitted to the  $11.8$  and  $18.7 \mu\text{m}$  radial profiles (Fig. 7). The unresolved component is the dominant contribution, accounting for  $\sim 70$ – $80\%$  of the total VISIR flux at those wavelengths. Deriving the nuclear fluxes by direct photometry in small apertures lead to similar values. The VISIR total flux at  $18.7 \mu\text{m}$  (Table 2) is in very good agreement with the  $18.3 \mu\text{m}$  flux reported by Packham et al. (2005), both measured in a 5 arcsec diameter aperture. The difference is less than 5%. That at  $11.8 \mu\text{m}$  is also in good agreement, 5% difference, with the  $12 \mu\text{m}$  flux measured in the ESO-3.6m /TIMMI2 spectrum presented in Siebenmorgen et al. (2004). However, Galliano et al. (2005) reports a total flux with TIMMI2 in the N-broad-band filter of about 45 % higher which we do not understand considering these observations are contemporaneous with those of Siebenmorgen et al.

The contribution of the extended emission component in Circinus is not negligible in absolute terms, the corresponding fluxes are at the level of a few janskys at the observed VISIR wavelengths (Table 3). Comparing with *IRAS* fluxes, the unresolved source at both VISIR wavelengths accounts for 40 to 20% of the  $12 \mu\text{m}$  and  $25 \mu\text{m}$  *IRAS* fluxes respectively. As in most objects in the sample, the IR light of the galaxy dominates over that of the AGN, the relevance of this contribution becoming higher with increasing wavelength as revealed by the spectral energy distribution of this nucleus (Prieto et al. 2009).

#### 4.12 NGC 7469

NGC 7469 is an SAb galaxy with a Seyfert 1 nucleus surrounded by a starburst ring at a radius of  $\sim 1$  arcsec from the center (300 pc). The current VISIR images at  $11.8$  and  $18.7$  are deeper show a very bright nucleus and several clumps from the star-forming ring (Fig. 10). The ring is better contrasted in the residual images (the central two-blob features in both residual images are caused by a PSF mismatch, Sect. 3.1).

Nuclear fluxes were derived from direct aperture photometry on the images following the procedure described in Sect. 3.3. A composite point-like source plus a disc model (Sect. 3.3) fit to the radial profiles was found not adequate because of the presence of the star-forming ring. Nevertheless, despite of this additional contribution not accounted for in the fit, the nuclear fluxes derived from the radial profile fit turn to be slightly larger than those from the aperture photometry. The total integrated flux - i.e., including the nucleus and the stellar ring, Table 3 - at  $11.88 \mu\text{m}$  differs by less than 10% from that by Galliano et al. (2005) who uses ESO-3.6m / TIMMI2 and the broad band filter centred at  $11.9 \mu\text{m}$  ( $\text{FWHM} = 2.26 \mu\text{m}$ ).

The emission from the star-forming ring was estimated as the difference between the total integrated flux in the image and that of the nucleus. This represents about half of

the total integrated emission (Table 3), and some emission from the ring may still be lost due to the limited nod throw of these observations, 8 arcsec. Thus, the star-forming ring is at least as powerful as the AGN. The corresponding AGN contribution to the *IRAS* flux is relatively small, from 40% at  $11.8 \mu\text{m}$  to 20% at  $18.7 \mu\text{m}$  of the  $12$  and  $25 \mu\text{m}$  fluxes respectively. Thus, the remaining *IRAS* flux at  $11.8 \mu\text{m}$  most plausibly comes in this galaxy from the star forming ring.

#### 4.13 NGC 7582

NGC 7582 is an SB galaxy with a Seyfert type 2 nucleus with broad recombination lines in the IR (Reunanen, Kotilainen & Prieto 2003). Several star-forming regions within a few arcseconds from the nucleus are seen along the west side of the nucleus Prieto, Reunanen, & Kotilainen (2002). These regions form indeed part of a circumnuclear ring in which more than twenty independent regions have being isolated in VLT/NACO adaptive optics images at  $2 \mu\text{m}$  (Fernandez-Ontiveros et al., in preparation). The  $[\text{O III}] 5007 \text{ \AA}$  gas follows a cone-like morphology on the west side of the nucleus (Storchi-Bergmann & Bonatto 1991), outlined in Fig. 10. The VISIR images show a prominent nucleus, several star-forming regions from the ring and diffuse emission, the latter being better contrasted in the residual images. A VISIR image taken with a filter centered on the  $[\text{Ne II}] 12.81 \mu\text{m}$  line plus continuum Wold & Galliano (2006) reveals a similar morphology.

As in NGC 7469, the nuclear fluxes are also here derived from direct aperture photometry on the images following the procedure described in Section 3.3. The composite PSF plus a disc model yields a poor fit at radii  $r \simeq 0.4$  arcsec (Fig. 10). We note, however, that the nuclear fluxes derived from a formal fit to the radial profile differ by  $\sim 5\%$  at  $11.8 \mu\text{m}$  and  $\sim 9\%$  at  $18.7 \mu\text{m}$ , with respect to those derived from the aperture photometry. The emission from the star-forming ring was then estimated as the difference between the total integrated flux in the image and that of the nucleus (Table 3).

As in NGC 7469, the contribution from the star-formation ring is as important as that of the AGN. In particular, the emission at  $18.7 \mu\text{m}$  is almost a factor 3 larger than that of the AGN. As compared with *IRAS*, the AGN represents  $\sim 30\%$  of the  $12 \mu\text{m}$  *IRAS* flux and  $< 10\%$  of  $25 \mu\text{m}$  *IRAS* flux.

## 5 DISCUSSION AND CONCLUSIONS

The mid-IR observations presented in this work, reaching spatial resolutions down to  $\text{FWHM} \sim 0.3$  arcsecs, allow us to constrain the AGN emission at mid-IR wavelengths within regions of 35 pc size in diameter on average (range from 5 to 130 pc). Within the central kpc region, most of the emission is concentrated in the nuclear region, and in most cases the bulk of it is linked to an unresolved component. Considering the physical scales sampled in these AGN, the outer radius of the torus at mid-IR wavelengths should on average be less than 18 pc, less than 4 pc in Circinus, this being the only galaxy in the sample with a detected parsec scale disc-like structure at its centre at near- and mid-IR

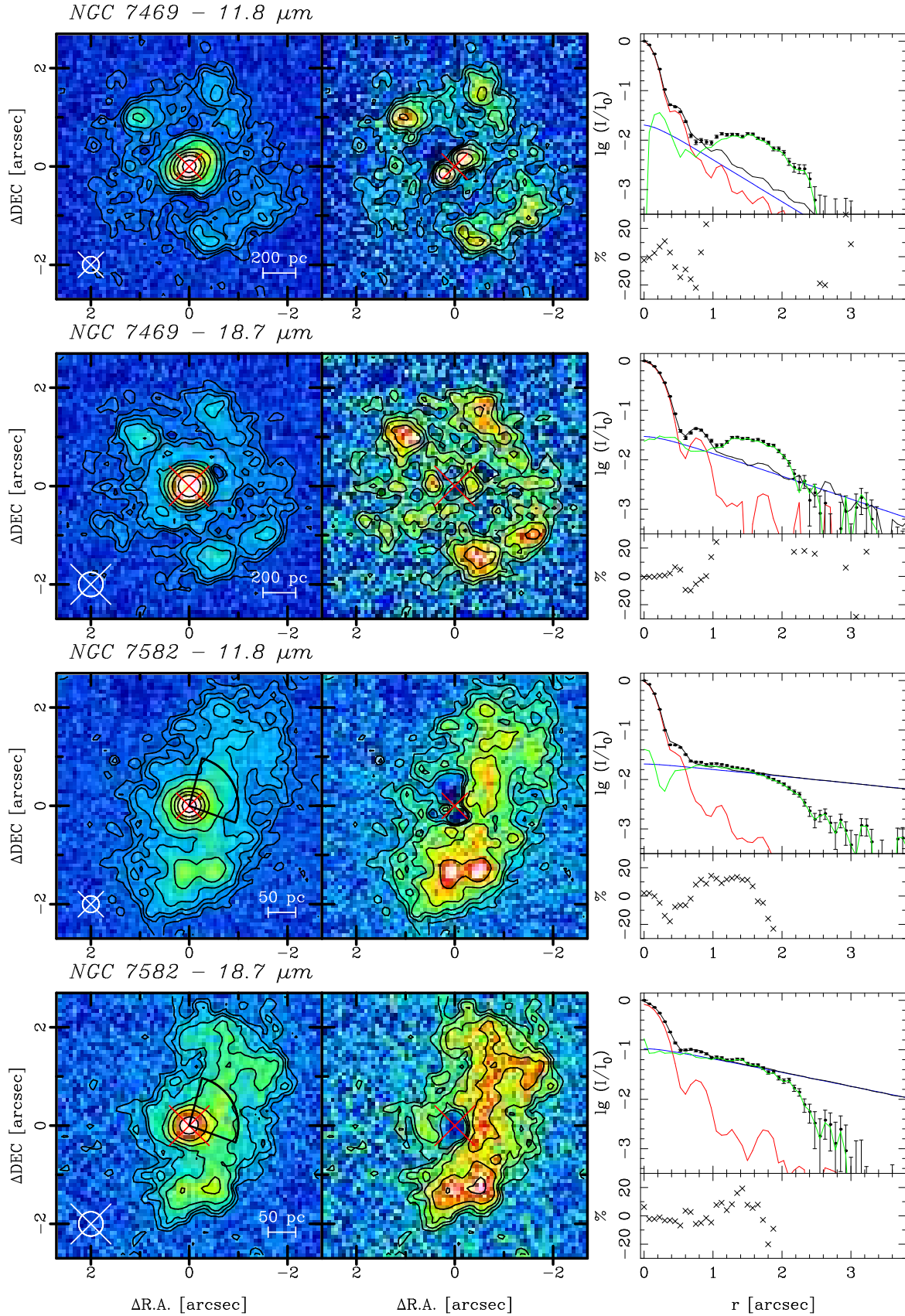


**Figure 10.** As in Fig. 2. The green line is the difference between total emission and fitted point-like source. The location of the ionization cone in NGC 7582 is outlined.  $1\sigma$  level is  $27\text{ mJy arcsec}^{-2}$  at 11.8,  $65\text{ mJy arcsec}^{-2}$  at 18.7  $\mu\text{m}$ , for NGC 7469;  $17\text{ mJy arcsec}^{-2}$  at 11.8,  $60\text{ mJy arcsec}^{-2}$  at 18.7  $\mu\text{m}$ , for NGC 7582.

wavelengths. Resolved or extended emission is detected in most of the objects within a few arcsec of the centre. The measured contribution of this extended component is a lower limit as part of the emission, particularly if diffuse, may easily be subtracted out in ground-based chopped observations. Further detection of emission from the galaxy is severely limited by the nod-throw of these observations, typically in the range of 8–10 arcsec.

On the basis of thirteen AGN studied, the following results are found:

(i) In three AGN (NGC 7582, NGC 7469 and NGC 1097), strong circumnuclear star-forming regions within a few arcsec from the centre are detected. These are located at radii of  $\sim 130$  pc in NGC 7582, 600 pc in NGC 1097 and 900 pc in NGC 7469. In all cases, their associated emission is comparable with, or even larger than, that of the AGN, particularly at  $18.7 \mu\text{m}$ .

(ii) In six further AGN, extended emission on scales from 1 to 3 arcsec from the centre is detected. This emission is preferentially distributed along a particular direction, usually coinciding with the ionization cone or the jet direction. In all cases, this contribution represents a few per cent of the AGN flux.

(iii) Only in four AGN the emission is concentrated into a central unresolved source, and in one galaxy, the Sombrero, no detection is reached.

(iv) In comparing the present photometry with previous works, most centered at  $\sim 11 \mu\text{m}$  and using broad filters that include PAH features, differences up to 15 to 20% in some cases which may be attributed to the contribution of PAH features are found; in M87 and NGC 5507 the agreement is within 5% indicating the absence of PHA features in these nuclei and hence of active star formation. Only in NGC 1097 and Cen A, whose nuclear spectrum does not present PAH features, genuine variability by a factor of 2 at  $11.8 \mu\text{m}$  in a time scale of 1 to 4 years respectively is indicated.

In the six AGN with extended emission about the centre, that appears tightly collimated. In Cen A and M87, it is aligned with the jet (in M87, it coincides with the brightest jet knot, HST-1). In Circinus, NGC 1386, and NGC 3783 the extended emission is co-spatial with the extended ionized gas. Only in NGC 5506, the extended component spreads along the mid-plane of the galaxy being perpendicular to the optical ionization cone main axis. The mid-IR filters used in this work, narrow and centred on windows where emission lines or PAH features are unimportant, are thus targeted to measure pure continuum emission. Thus, the extended emission in M87 and Cen A is presumably of synchrotron origin; in all other cases, its nature is more ambiguous. Possibilities include free-free emission due to cooling of the ionized gas in the ionization cone (Contini, Viegas, & Prieto 2004), or/and emission from dust heated by the AGN. Considering the intrinsic AGN luminosities of these objects, inferred from either high spatial resolution IR spectral energy distribution (Prieto et al. 2007, 2009):  $\sim 8 \times 10^{42}$  erg/sec in Circinus;  $\sim 4 \times 10^{44}$  erg/sec in NGC 3783, or X-ray data;  $\sim 1.3 \times 10^{42}$  erg/sec in NGC 1386 (Levenson et al. 2006), and the distances at which mid-IR emission is detected – in the range of 30 pc in Circinus, to 400 pc in NGC 3783 (see Table 3) – the nature of this emission could be reconciled with dust directly heated by the AGN provided its equilib-

rium temperature is in the 100 K range (Barvainis’s 1987 formalism is assumed).

The contribution of free-free emission in the mid-IR could also be important if strong shocks exciting the gas are occurring (see, for example, fig. 2c of Contini & Viegas-Aldrovandi 1990). Evidence for high gas velocities in the above objects is inferred from the kinematic analysis of their high ionization coronal lines. Specifically, the FWHM of [Fe-VII] 6087 Å is  $\sim 400 \text{ km s}^{-1}$  in Circinus and  $\sim 1400 \text{ km s}^{-1}$  in NGC 1386 and NGC 3783 (Rodríguez-Ardila et al. 2006). Moreover, the size of the extended mid-IR emission closely coincides with the observed sizes of the Fe or Si coronal region (Rodríguez-Ardila et al.) and with their spatial location, which indicates that a fraction of the mid-IR emission is due to free-free emission from predominantly shock-heated coronal gas. Estimating this contribution requires detailed modelling and is currently being explored.

Mid- and far-IR emission of galaxies is usually derived from large-aperture data obtained by IR satellites. For galaxies with an AGN, it is widely assumed that most of this emission comes from the nucleus. The flux level of the nuclear point source in the AGN studied in this work proves the assumption to be inadequate in most cases. The estimated  $11.8$  and  $18.7 \mu\text{m}$  nuclear fluxes are larger, by factors of  $> 3$ , than the fluxes measured by *IRAS* at  $12$  and  $25 \mu\text{m}$  in 70% of the sample, the largest discrepancy being more than an order of magnitude in five galaxies: NGC 1097, NGC 1566, M87, Cen A and NGC 7582 (in the latter case only at  $18.7 \mu\text{m}$ ). In the remaining 30% of the sample, the *IRAS* flux levels are still larger but within a factor of 2.

The “extra” IR excess measured by *IRAS* has to come from a source other than the AGN, either strong IR sources, presumably located outside the central  $20 \text{ arcsec} \times 20 \text{ arcsec}$  region – common f.o.v. in ground-based mid-IR observations – or from a more extended low surface brightness component across the galaxy. For example, in the three AGN with circumnuclear star-forming regions, the total integrated emission (AGN plus star-forming ring) accounts for the *IRAS* flux levels within a factor of 2. This is the case of NGC 7582 and NGC 7469; in NGC 1097, the difference is still a factor 10, but in this case the VISIR f.o.v. does not map the complete extension of the ring. In all other AGN with detected nuclear extended emission, this contribution is minor, albeit a lower limit because of the lower sensitivity imposed by chopped observations. The overall conclusion based on this small sample is that in AGN with strong circumnuclear star formation, this component can well account for most of the *IRAS* flux. For all other cases, either a low surface brightness component extending over galactic scales or strong extranuclear IR sources – e.g. H II regions in spiral arms – are the major contribution to the IR light of these galaxies. In either case, the contribution of these components surpasses by large factors to orders of magnitude that of the AGN at mid-IR wavelengths.

## 6 ACKNOWLEDGEMENTS

JR acknowledges financial support from the Academy of Finland (projects 8121122, 8127055).



## REFERENCES

- Baribaud T., Alloin D., Glass I., Pelat D., 1992, *A&A*, 256, 375
- Barvainis R., 1987, *ApJ*, 320, 537
- Beckert T., Driebe T., Höning S. F., Weigelt G., 2008, *A&A*, 486, L17
- Bendo G. J., et al., 2006, *ApJ*, 645, 134
- Contini M., Viegas S. M., Prieto M. A., 2004, *MNRAS*, 348, 1065
- Dale D. A., et al., 2007, *ApJ*, 655, 863
- Ferrarese L., Mould J. R., Stetson P. B., Tonry J. L., Blakeslee J. P., Ajhar E. A., 2007, *ApJ*, 654, 186
- Ferruit P., Wilson A. S., Mulchaey J., 2000, *ApJS*, 128, 139
- Freeman K. C., Karlsson B., Lynga G., Burrell J. F., van Woerden H., Goss W. M., Mebold U., 1977, *A&A*, 55, 445
- Galliano, E., Alloin, D., Pantin, E., Lagage, P.O. & Marco, O., 2005, *A&A*, 438, 803
- Glass I. S., 2004, *MNRAS*, 350, 1049
- Häring-Neumayer N., Cappellari M., Rix H.-W., Hartung M., Prieto M. A., Meisenheimer K., Lenzen R., 2006, *ApJ*, 643, 226
- Haas, M. et al. 2007, *A&A* 473, 369
- Harris D. E., Cheung C. C., Biretta J. A., Sparks W. B., Junor W., Perlman E. S., Wilson A. S., 2006, *ApJ*, 640, 211
- Israel F. P., 1998, *A&ARv*, 8, 237
- Lagage P. O., et al., 2004, *Msngr*, 117, 12
- Levenson N. A., Heckman T. M., Krolik J. H., Weaver K. A., Życki P. T., 2006, *ApJ*, 648, 111
- Madore B. F., et al., 1999, *ApJ*, 515, 29
- Maiolino R., Alonso-Herrero A., Anders S., Quillen A., Rieke M. J., Rieke G. H., Tacconi-Garman L. E., 2000, *ApJ*, 531, 219
- Maiolino R., Ruiz, M., Rieke, G. H., Keller, L. D. 1995, *ApJ* 446, 661
- Marshall H. L., Miller B. P., Davis D. S., Perlman E. S., Wise M., Canizares C. R., Harris D. E., 2002, *ApJ*, 564, 683
- Mason R. E., Levenson N. A., Packham C., Elitzur M., Radomski J., Petric A. O., Wright G. S., 2007, *ApJ*, 659, 241
- Meisenheimer K., et al., 2007, *A&A*, 471, 453
- Moshir M., et al., 1990, *IRAS Faint Source Catalogue*, version 2.0
- Mueller Sánchez F., Davies R. I., Eisenhauer F., Tacconi L. J., Genzel R., Sternberg A., 2006, *A&A*, 454, 481
- Mulchaey, J., Wilson, A. & Tsvetanov, Z., 1996. *ApJSS* 102, 309
- Packham C., Radomski J. T., Roche P. F., Aitken D. K., Perlman E., Alonso-Herrero A., Colina L., Telesco C. M., 2005, *ApJ*, 618, L17
- Orienti, M. & Prieto, M. A., 2009, *MNRAS* in press
- Perlman E. S., Sparks W. B., Radomski J., Packham C., Fisher R. S., Piña R., Biretta J. A., 2001, *ApJ*, 561, L51
- Prieto M. A., Reunanen J., Beckert T., Tristram K., Neumayer N., Fernandez J. A., Acosta J., 2007, *ASPC*, 373, 600
- Prieto M. A., Maciejewski W., Reunanen J., 2005, *AJ*, 130, 1472
- Prieto M. A., et al., 2009, *MNRAS* in press
- Prieto M. A., et al., 2004, *ApJ*, 614, 135
- Prieto M.A., Marco O., Gallimore J., 2005, *MNRAS*, 364, L28
- Prieto M. A., Reunanen J., Kotilainen J. K., 2002, *ApJ*, 571, L7
- Ramos Almeida C., Pérez García A. M., Acosta-Pulido J. A., Rodríguez Espinosa J. M., 2007, *AJ*, 134, 2006
- Reunanen J., Kotilainen J. K., Prieto M. A., 2003, *MNRAS*, 343, 192
- Rodríguez-Ardila A., Prieto M. A., Viegas S., Gruenwald R., 2006, *ApJ*, 653, 1098
- Schmitt H. R., Kinney A. L., 1996, *ApJ*, 463, 498
- Schmitt H. R., Donley J. L., Antonucci R. R. J., Hutchings J. B., Kinney A. L., 2003, *ApJS*, 148, 327
- Siebenmorgen R., Krügel E., Spoon H. W. W., 2004, *A&A*, 414, 123
- Siebenmorgen R. et al., 2008, *A&A*, 488, 83
- Storchi-Bergmann T., Bonatto C. J., 1991, *MNRAS*, 250, 138
- Tokovinin A., Sarazin M., Smette A., 2007, *MNRAS*, 378, 701
- Tristram K. R. W., et al., 2007, *A&A*, 474, 837
- Tristram K. R. W. et al. 2009, *A&A* in press
- Veilleux S., Goodrich R. W., Hill G. J., 1997, *ApJ*, 477, 631
- Wilson A. S., Shopbell P. L., Simpson C., Storchi-Bergmann T., Barbosa F. K. B., Ward M. J., 2000, *AJ*, 120, 1325
- Whysong D., Antonucci R., 2004, *ApJ*, 602, 116
- Wold M., Galliano E., 2006, *MNRAS*, 369, L47